Efficient and tunable one-dimensional charge transport in layered lanthanide metal–organic frameworks

Grigorii Skorupskii [1], Benjamin A. Trump[2], Thomas W. Kasel [3], Craig M. Brown [2,4], Christopher H. Hendon [3] and Mircea Dincă [1]*

The emergence of electrically conductive metal–organic frameworks (MOFs) has led to applications in chemical sensing and electrical energy storage, among others. The most conductive MOFs are made from organic ligands and square-planar transition metal ions connected into two-dimensional (2D) sheets stacked on top of each other. Their electrical properties are thought to depend critically on the covalency of the metal–ligand bond, and less importance is given to out-of-plane charge transport. Here, we report a series of lanthanide-based MOFs that allow fine tuning of the sheet stacking. In these materials, the Ln^{3+} ions lie between the planes of the ligands, thus connecting organic layers into a 3D framework through lanthanide–oxygen chains. Here, efficient charge transport is found to occur primarily perpendicular to the 2D sheets. These results demonstrate that high conductivity in layered MOFs does not necessarily require a metal–ligand bond with highly covalent character, and that interactions between organic ligands alone can produce efficient charge transport pathways.

Electrically conductive metal–organic frameworks (MOFs) have recently attracted attention as potential materials for supercapacitors[1,2], batteries[3], thermoelectric devices[4], chemiresistive sensors[5,6] and electrocatalysts[7–10]. Significant effort has been devoted towards the development of MOFs with increasingly high conductivities[11,12]. Current record values of 2,500 S cm^{-1} at room temperature for non-porous coordination polymers[13] and 40 S cm^{-1} for porous MOFs[14], with many others approaching them[15–17], have been reported in hexagonal layered frameworks based on hexa-substituted triphenylenes and benzenes connected by first-row divalent transition metal ions such as Ni^{2+} and Cu^{2+}. The high conductivity values of these materials are often attributed to the strong in-plane conjugation between the π-systems of the ligands and the d orbitals of the metals[18–21]. Because of this assumption, to our knowledge there are no studies of charge transport normal to the metal–organic sheets. Despite attempts to make two-dimensional (2D) MOFs with metal–ligand bonding showing varying degrees of covalency[22]—which could answer fundamental questions related to charge transport in these materials—there are no reports on the details of their structures or electronic properties.
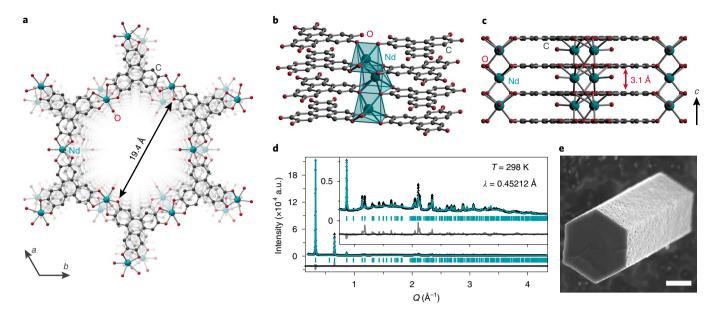
One class of metal ions that is well suited for systematic investigations of structure–function relationships is the lanthanides. In their trivalent states, lanthanide ions (Ln^{3+}) have empty $5d$ shells, with all valence electrons lying in heavily shielded, deep $4f$ orbitals. Because the $4f$ orbitals do not participate significantly in bonding, Ln^{3+} ions typically form considerably more ionic compounds than transition metals[23]. This is attractive for MOF syntheses, where more labile, reversible bonds form more crystalline materials, which is crucial for attaining systematic control over the electronic structure of the materials. One added benefit of using Ln^{3+} to target conductive MOFs is their nearly identical chemical behaviour stemming from their ionicity, and their otherwise very different ionic

radius, which decreases by more than 15% from La^{3+} to Lu^{3+} (ref. [24]). These properties make them ideal for studying structure–function correlations where covalency is essentially decoupled from structural considerations.

Here, we report a family of MOFs made from Ln^{3+} and 2,3,6,7,10,11-hexahydroxytriphenylene (H_6HHTP). Although the more ionic bonding between Ln^{3+} and the catecholate ligands may be expected to diminish the efficiency of charge transport within the 2D plane, the materials exhibit conductivity values reaching 0.05 S cm^{-1} in two-probe polycrystalline pellet measurements, on par with the most conductive MOFs reported so far[11,12,25]. The high crystallinity of the materials allows systematic control of structural parameters and reveals a direct correlation between the stacking distance, the conductivity and the optical bandgap of MOFs made from four different lanthanides spanning the entire $4f$ series.

Results and discussion

Synthesis and structural characterization. A solvothermal reaction of H_6HHTP with hydrated $Ln(NO_3)_3$ (Ln = La, Nd, Ho, Yb) in a mixture of water and N,N'-dimethylimidazolidinone (DMI) produced dark green–blue microcrystalline powders of $Ln_{1+x}HHTP(H_2O)_n$ ($x=0$ to 0.2; referred to as **LnHHTP**). Scanning electron microscopy (SEM) showed that the powders consisted of well-shaped hexagonal needles (Fig. 1e and Supplementary Fig. 1), varying in length between 1 μm and 200 μm depending on the exact synthetic conditions. Although sufficiently long, these crystals were not sufficiently thick for single-crystal X-ray diffraction studies. Their structures were instead obtained by Rietveld refinement[26] of powder X-ray diffraction (PXRD) data, which provided excellent structural models for the Nd^{3+} (Fig. 1) and Yb^{3+} analogues (Supplementary Fig. 19). The two materials are isostructural, with differences in unit cell parameters and Ln–O bond lengths attributable to the smaller size

Fig. 1 | Structure of NdHHTP. a–c, A representation of the crystal structure of **NdHHTP**, viewed along the *c* direction, and displaying the crystallographic pore diameter (**a**), the metal–ligand connectivity of the seven-coordinate Nd atoms (**b**) and the layer stacking (**c**). Hydrogen atoms are omitted for clarity. The structure is similar to related transition metal-based materials, but the Nd atoms connect the ligand layers into a 3D framework and force the organic layers significantly closer together. **d**, Rietveld refinement of the average **NdHHTP** structure to synchrotron PXRD data. Experimental data are shown as black triangles, the model fit in teal and the difference curve in grey. The tick marks denote the calculated peak positions. Fit statistics were $R_p = 5.80\%$, $R_{wp} = 7.74\%$ and GoF $= 3.73$. Triangle sizes are commensurate with error bars from standard deviations. **e**, SEM image of a **NdHHTP** crystal. Scale bar, 1 μm.

of Yb^{3+} compared to Nd^{3+}. Both structures show two-site disorder, each exhibiting two sets of equally occupied ligand and metal sites. For clarity, Fig. 1 presents only one half of the averaged, disordered **NdHHTP** structure. Similar to the reported transition metal analogues, Ln^{3+} ions bind the triangular **HHTP** ligands into honeycomb-like 2D nets featuring solvent-accessible pores with a crystallographic diameter of ~1.94 nm for **NdHHTP**. The experimental pore diameters of all four materials (Supplementary Fig. 10), measured by fitting N_2 adsorption isotherms at 77 K (Supplementary Figs. 6–9)[27], were found to be ~1.6 nm, in line with the crystallographic values. The same N_2 adsorption isotherms gave Brunauer–Emmett–Teller (BET)[28] surface areas of 200–510 $m^2\,g^{-1}$, also in good agreement with the values reported for the related 2D *d*-metal-based MOFs (490 $m^2\,g^{-1}$ for the Co-based framework Co-CAT-1 and 425 $m^2\,g^{-1}$ for the Ni-based framework Ni-CAT-1)[17].

Importantly, whereas transition metals lie in the same plane as the organic ligands and form strictly 2D sheets, here the Ln^{3+} ions lie between the planes of the organic ligands, thereby connecting the latter into a 3D network. The lanthanides themselves are bound to six oxygen atoms from neighbouring ligands and one water or hydroxide group. They are bridged into infinite chains that can be represented as edge-sharing capped trigonal prisms, bearing resemblance to the coordination environment and extended structure of rare-earth oxides, including Nd_2O_3 (Supplementary Fig. 18)[29]. The lanthanide sites are not fully occupied in either **NdHHTP** or **YbHHTP**, with almost a third of the positions empty, as would be expected based on the formula unit. A more detailed structural description, including additional models of the location of empty lanthanide crystallographic sites is provided in Supplementary Information p. 7.
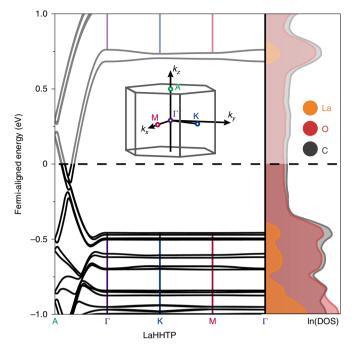
PXRD patterns for **LaHHTP** and **HoHHTP** (Supplementary Fig. 11) are qualitatively identical to those of **NdHHTP** and **YbHHTP**, suggesting that all four materials are isostructural. Pawley refinements[30] on multiple batches of the four materials revealed a clear decrease in the unit cell parameters moving across the series from La^{3+} to Yb^{3+}, in line with a corresponding decrease in ionic

radii (Supplementary Fig. 17). Notably, the size difference between the early and late lanthanides causes further reduction from an already short interlayer stacking distance of 3.068(2) Å for **LaHHTP** to a very short 3.002(6) Å for **YbHHTP**. Such close π-stacking is rarely seen in layered materials (Supplementary Table 2): in all other triphenylene-based MOFs the average layer spacing is larger than 3.3 Å (refs. [6,14,17]). Even in graphite itself, the layers are separated by 3.36 Å at room temperature[31], a distance more than 10% larger than that observed in **YbHHTP**.

Electronic band structure calculations. Excited by the possibility of the close π-stacking promoting efficient ligand orbital overlap in the crystallographic *c* direction, which could promote charge transport normal to the 2D sheets, we investigated the electronic structures of the materials by density functional theory (DFT). To avoid prohibitive computationally intensive spin-polarized calculations, we performed calculations on the closed-shell **LaHHTP** structure and a hypothetical **LuHHTP** structure as a model for the smaller lanthanides Yb^{3+} and Ho^{3+}. These calculations suggest that the materials should exhibit metallic behaviour along the *c* direction (A to Γ vector in the Brillouin zone in Fig. 2), as evidenced by the bands crossing the Fermi level. In contrast, the Fermi level lies inside a bandgap within the *a–b* plane (Γ-K-M), suggesting semiconductive behaviour in the plane parallel to the organic layers (Γ-K-M). As expected, lanthanide valence orbitals do not contribute significantly to bands around the Fermi level, suggesting that in-plane electronic communication between ligands is minimal. Indeed, the bands along the Γ-K-M vectors are essentially flat and form 'in-plane' band gaps of ~0.7–1.2 eV that are strongly dependent on the stacking distance (Supplementary Figs. 21 and 22). This is in stark contrast to the band structure along the A to Γ vector ('cross-plane'), where the bands are spread very widely and give rise to a low density of states (DOS). Furthermore, modelling structures with different metal atoms leads to insignificant changes in shifting from La to Lu. For more information on interpreting band structures, see refs. [32,33].
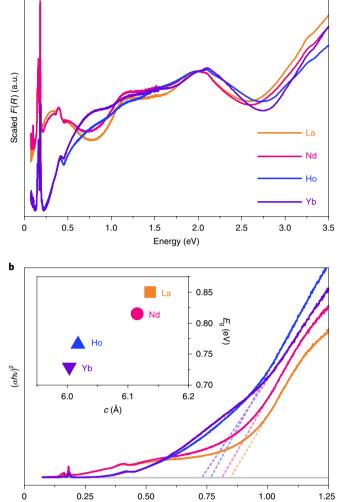
Fig. 2 | Electronic band structure and DOS of LaHHTP. Calculations include spin–orbit coupling effects. Significant band curvature in the A to Γ direction indicates strong interaction between the layers. Additionally, the Fermi level crosses the bands in this direction, suggesting metallicity. The DOS is plotted in logarithmic coordinates to emphasize the non-zero density at the Fermi level, and shows the much lower contribution of La to the frontier bands. The inset shows the first Brillouin zone—the primitive cell of the reciprocal lattice—to help guide the reader through the wavevector positions within the band diagram.

Optical spectroscopy. Diffuse reflectance spectra for the four materials (Fig. 3a) show clear absorption edges in the 0.7–1 eV range, which we assign as the 'in-plane' gap predicted by DFT calculations. The four MOFs also show absorption features below this edge, at ~0.3 eV for La and Nd, and at ~0.7 eV for Ho and Yb. These absorption features, however, do not conform to a linear region when plotted on a Tauc plot[34] for direct or indirect bandgaps, and can therefore be attributed to absorption by defects. Unambiguous identification of these defects is beyond the scope of the current work, but possibilities include the following: metal vacancies, as supported by PXRD analysis; ligand vacancies, which DFT confirms as possibly giving rise to such absorption features (see Supplementary Information p. 10 for more details); mixed-valent states within the ligand set. This last possibility is supported by prior work, where absorption features at 2,000–3,000 nm in a $[Ru_3HHTP]^{2+}$ complex were attributed to intra-ligand charge transfer[35]. Plotted in Tauc coordinates for direct allowed transitions (Fig. 3b), the spectra reveal a surprising trend of narrowing optical bandgaps in transitioning from the larger lanthanides, 0.85 eV for **LaHHTP**, to the smaller ones, 0.73 eV for **YbHHTP**. This trend is opposite to what is observed in most classical semiconductors, including GaAs[36], InP[37] and Ge[38], where pressurization and decreasing unit cell parameters lead to widening bandgaps. The trend in **LnHHTP** materials conforms, however, to what is observed for semiconductors such as PbE (E = S, Se, Te), where band inversion occurs[39], as well as for some indirect-gap semiconductors, including Si[38]. The precise assignment of this trend warrants further systematic experiments. We note, however, that the DFT calculations here position the Fermi energy at a ligand oxidation of $HHTP^{3-}$, whereas the experimental formula indicates slight variations of this oxidation state towards more reduced ligands, which would shift the Fermi energy higher.
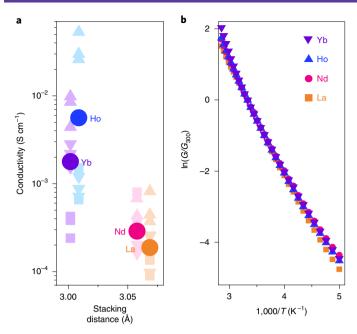

Fig. 3 | Diffuse reflectance spectra for LnHHTP (Ln = La, Nd, Ho and Yb). **a**, Kubelka–Munk transforms ($F(R)$) of the spectra, showing significant absorption extending into the infrared region. **b**, The same data but plotted in Tauc coordinates for direct allowed transitions. Pale dashed lines show extrapolation of the linear fit regions. The optical bandgaps of the materials can be obtained as the abscissa intercepts of the dashed lines. A grey line that follows $(\alpha h\nu)^2 = 0$ is added to aid the reader, where α is the absorption coefficient of the material, h is Planck's constant and ν is the wavelength of light. The inset shows the variation of the estimated optical bandgaps of the four materials with the unit cell parameter c.

Electrical conductivity. The electrical conductivities of polycrystalline pellets made from **LnHHTP** materials are on par with the most conductive porous MOFs to date, ranging from $0.9 \times 10^{-4}\,\mathrm{S\,cm^{-1}}$ for **LaHHTP** to $0.05\,\mathrm{S\,cm^{-1}}$ for **HoHHTP** at 29 °C (Fig. 4a). Although relatively wide batch-to-batch variation is observed for each material, higher averages and higher device conductivities are consistently achieved for the smaller lanthanides (Ho, Yb), which produce the more densely stacked structures. The conductivity of **HoHHTP** pellets, $0.05\,\mathrm{S\,cm^{-1}}$, is within the range of the most conductive 3D connected MOFs to date[25], which is noteworthy given the low degree of covalency provided by Ln−O bonds in **LnHHTP** materials[23]. Importantly, the values for all **LnHHTP** MOFs are probably significantly underestimated due to the potentially anisotropic nature of charge transport, as well as additional contact and grain boundary resistances[11]. Although these contributions are difficult to

Fig. 4 | Electrical conductivity of LnHHTP (Ln = Yb, Ho, Nd and La).
a, Two-probe pressed pellet conductivities measured at 29 °C. Squares, downward-facing triangles and upward-facing triangles denote three independent batches of each material. Each point marks an individual pellet measurement. Circles mark average values. **HoHHTP** and **YbHHTP**, where the organic interlayer distance is shorter, consistently show higher conductivities than **LaHHTP** and **NdHHTP**, where the stacking distances are larger. **b**, Temperature dependence of the normalized conductance G/G_{300} of **LnHHTP** in Arrhenius coordinates, where G_{300} is the conductance at 300 K (Supplementary Figs. 34–37). The four materials show similar temperature-activated conductivity behaviour.

quantify, they are assumed to be reasonably similar for the different materials because all MOFs present similar morphologies and crystallite size (Supplementary Fig. 44). Conductivity improvements of more than two orders of magnitude have been reported for single-crystal measurements of MOFs compared to two-probe pellets[40].

Variable-temperature conductivity measurements revealed thermally activated transport for the four studied materials (Fig. 4b). Fitting the conductance versus temperature data to the Arrhenius equation $G = G_0 \exp\left(\frac{E_A}{kT}\right)$, where G is the conductance, G_0 is a prefactor, E_A is the activation energy, k the Boltzmann constant and T the temperature, in the temperature range 225–300 K, revealed similar E_A values of ~0.25 eV for all four materials (Supplementary Figs. 34–37). These values are in line with those reported for other highly conductive MOFs, including chemically related 2,5-dihydroxybenzoquinone and chloranilic acid-based materials[21,41]. Although thermally activated transport is a defining characteristic for semiconducting materials[33], appearing to contradict the calculated band structures, grain boundaries can dominate electrical transport behaviour in polycrystalline pellets[15]. We also note that the DFT calculations predict metal-like transport to be anisotropic along the c direction, with semiconducting behaviour in the $a–b$ plane. Because the DOS at the Fermi level is significantly lower than in the region of the 'in-plane' bands, transport in these materials may intrinsically display some degree of thermal activation. Defect states that we observe both by X-ray diffraction, in the form of the cationic vacancies, and by diffuse-reflectance spectroscopy can also change transport behaviour from metallic to semiconducting, as has been shown in the literature[42]. Additionally, our DFT calculations on **LaHHTP** with linker vacancies (Supplementary Figs. 47 and 48) show localization of the ligand electronic wavefunction,

forming flat bands around the Fermi level. Although the simulated (that is, ideal) defective material maintains its metallicity through the undisrupted ligand stacks, local transport through the missing linker defects would presumably be thermally activated.

Outlook

With the most intense current interest in 2D materials focused on 'in-plane' electronic properties, the 'out-of-plane' transport properties have received comparatively less attention. In contrast with traditional inorganic 2D materials, MOFs lend themselves to facile ligation to produce functional materials with 2D layers connected by strong bonds. We demonstrate that reacting lanthanide cations with ligands traditionally used for synthesizing conducting 2D MOFs leads to layered materials where organic ligands form sheets with insignificant in-plane electronic communication. Electrical transport instead occurs primarily normal to the plane and is highly modulated by the inter-sheet stacking distance, which in turn varies proportionally with the size of the lanthanide cation. These results offer an alternative point of view to the canonical interpretation of transport in conductive 2D MOFs, which has focused almost entirely on 'in-plane' arguments. Our findings enlarge the spectrum of possible interactions that can give rise to efficient transport in these porous materials, thereby providing an additional design strategy towards MOFs with record conductivities and charge delocalization in all three dimensions.

Methods

Synthesis of LnHHTP (Ln = La, Nd, Ho and Yb). In air, to a 20 ml scintillation vial containing a solution of 0.629 mmol (10.0 equiv.) Ln(NO$_3$)$_3$·nH$_2$O in 3.0 ml deionized water, a solution of 0.063 mmol (1.0 equiv., 20 mg) **H$_6$HHTP** in 0.4 ml DMI was added. A solution of 0.189 mmol (3.0 equiv., 15 mg) anhydrous sodium acetate in 0.6 ml deionized water was added to the mixture, inducing the formation of a cloudy grey precipitate. The vial was capped and left at 80 °C for 16 h, during which the precipitate slowly turned green and then dark blue. The precipitate was collected by centrifugation, and transferred to a N$_2$-filled glove box containing, but not saturated with, water vapour. The precipitate was soaked four times for at least 30 min in deionized water, followed by four times for at least 30 min in acetone (both solvents were degassed by freeze–pump–thawing three times). The vial containing the precipitate was then fitted with a vacuum adapter, and the precipitate was dried in vacuo on a Schlenk line for 1 h at 90 °C. For elemental analysis and N$_2$ adsorption measurements, the samples were dried overnight under the same conditions. The samples were then transferred into a dry N$_2$-filled glove box. No deterioration in the physical properties or the phase purity was observed over the course of at least four months. Prolonged exposure to air had no observed impact on the phase purity based on PXRD. Elemental analysis results are provided in the Supplementary Information p. 5.

Electrical conductivity measurements. Two-contact probe measurements were carried out at 302 K in a dry nitrogen-filled glove box on pressed pellets using a home-built two-point probe set-up, as described previously[40]. For each measurement, the powder was loaded into a glass tube and compressed between two stainless steel rods, which also served as current collectors. The cell was then transferred into a hydraulic press, and the press was tightened fast by hand. No additional pressure was applied. Linear $I–V$ curves were then obtained by sweeping the voltage and measuring the current using a source meter (Keithley 6517b or Keithley 2450) connected to the press with test leads. The voltage limits were chosen depending on the resistance of the pellet measured, but generally were between −0.5 V and +0.5 V. The cell was then allowed to stand pressurized for 10 min, then retightened, and $I–V$ curves were collected again. This process was repeated several times until the change in observed resistance was low (Supplementary Fig. 45). Pellet thicknesses were determined after the electrical measurements using a micrometer (Mitutoyo).

Variable-temperature conductivity data were collected using a Quantum Design PPMS DynaCool equipped with the Electrical Transport Option.

Computational methods. Beginning with the crystallographic structure of **NdHHTP**, models for **LaHHTP** and **LuHHTP** were built by substituting the metal atoms. The materials were then geometrically equilibrated using the DFT functional PBEsol[43] with plane-augmented-wave (PAW) pseudopotentials and an energy cutoff of 500 eV, as implemented in VASP[44]. Ln-bound O were single protonated to form the terminal hydroxide to achieve bulk charge neutrality. Scalar relativistic effects were included in the PAW pseudopotentials. The equilibrium geometry and electronic ground state were computed with ionic and electronic convergence criteria of 0.005 eV Å^{-1} and 10^{-6} eV, respectively, resulting in tightly converged structures.

Due to the large crystal system size of MOFs, a Γ-only k-grid was utilized during optimization. Electronic band structures and DOS plots were calculated using the PBEsol functional[43] with added spin–orbit coupling effects through inclusion of non-collinear electron spins on a higher resolution k-grid of $2\times2\times4$. The maximum band dispersion was found by sampling the intersheet direction, which had closest contacts of 2.98 Å for the optimized structure. For comparison, the DFT-D3 method of Grimme[45,46] and the same method as above were used to obtain a second equilibrium geometry, electronic band structure and DOS plot for **LaHHTP**. The results were qualitatively similar, with the dispersion correction resulting in an intersheet contraction (2.91 Å) and minor increase in band dispersion. The *c* spacing of the **LaHHTP** sheets was experimentally determined to be 3.1 Å, thus a third equilibrium geometry, electronic band structure and DOS plot were calculated for **LaHHTP** with an artificially increased *c* spacing matching experimental data. This system showed an expected reduction in band curvature, which typically scales inversely with interatomic distance. Additional band structures and DOS plots of both **LaHHTP** and **LuHHTP** excluding spin–orbit coupling effects and using the PW91 functional[47] were also examined. We were unable to geometrically equilibrate the spin-polarized Nd, Ho or Yb materials due to computational limitations.

Further information on the experimental and computational methods, structural details, SEM images, thermogravimetric analysis results, nitrogen adsorption isotherms, infrared spectra, Tauc plots, PXRD patterns, current–voltage characteristics, calculated band structures and variable temperature conductivity plots are provided in the Supplementary Information.

Data availability

Crystallographic information obtained by Rietveld refinement of PXRD data has been deposited in the Cambridge Crystallographic Data Centre under accession codes CCDC 1874834 (**NdHHTP**) and CCDC 1874835 (**YbHHTP**). All other data supporting the findings of this study are available within the article and its Supplementary Information, or from the corresponding author upon reasonable request.

Online content

Any Nature Research reporting summaries, source data, extended data, supplementary information, acknowledgements, peer review information; details of author contributions and competing interests; and statements of data and code availability are available at https://doi.org/10.1038/s41557-019-0372-0.

Received: 25 October 2018; Accepted: 9 October 2019;
Published online: 25 November 2019

References

1. Sheberla, D. et al. Conductive MOF electrodes for stable supercapacitors with high areal capacitance. *Nat. Mater.* **16**, 220–224 (2016).
2. Feng, D. et al. Robust and conductive two-dimensional metal–organic frameworks with exceptionally high volumetric and areal capacitance. *Nat. Energy* **3**, 30–36 (2018).
3. Wada, K., Sakaushi, K., Sasaki, S. & Nishihara, H. Multielectron-transfer-based rechargeable energy storage of two-dimensional coordination frameworks with non-innocent ligands. *Angew. Chem. Int. Ed.* **57**, 8886–8890 (2018).
4. Erickson, K. J. et al. Thin film thermoelectric metal–organic framework with high Seebeck coefficient and low thermal conductivity. *Adv. Mater.* **27**, 3453–3459 (2015).
5. Smith, M. K. & Mirica, K. A. Self-organized frameworks on textiles (SOFT): conductive fabrics for simultaneous sensing, capture and filtration of gases. *J. Am. Chem. Soc.* **139**, 16759–16767 (2017).
6. Campbell, M. G., Sheberla, D., Liu, S. F., Swager, T. M. & Dincă, M. Cu₃(hexa iminotriphenylene)₂: an electrically conductive 2D metal–organic framework for chemiresistive sensing. *Angew. Chem. Int. Ed.* **54**, 4349–4352 (2015).
7. Miner, E. M. et al. Electrochemical oxygen reduction catalysed by Ni₃(hexaim inotriphenylene)₂. *Nat. Commun.* **7**, 10942 (2016).
8. Miner, E. M. et al. Mechanistic evidence for ligand-centered electrocatalytic oxygen reduction with the conductive MOF Ni₃(hexaiminotriphenylene)₂. *ACS Catal.* **7**, 7726–7731 (2017).
9. Miner, E. M., Wang, L. & Dincă, M. Modular O₂ electroreduction activity in triphenylene-based metal–organic frameworks. *Chem. Sci.* **9**, 6286–6291 (2018).
10. Clough, A. J., Yoo, J. W., Mecklenburg, M. H. & Marinescu, S. C. Two-dimensional metal–organic surfaces for efficient hydrogen evolution from water. *J. Am. Chem. Soc.* **137**, 118–121 (2015).
11. Sun, L., Campbell, M. G. & Dincă, M. Electrically conductive porous metal–organic frameworks. *Angew. Chem. Int. Ed.* **55**, 3566–3579 (2016).
12. Stassen, I. et al. An updated roadmap for the integration of metal–organic frameworks with electronic devices and chemical sensors. *Chem. Soc. Rev.* **46**, 3185–3241 (2017).
13. Huang, X. et al. Superconductivity in a copper(II)-based coordination polymer with perfect kagome structure. *Angew. Chem. Int. Ed.* **57**, 146–150 (2018).
14. Sheberla, D. et al. High electrical conductivity in Ni₃(2,3,6,7,10,11-hexaiminotriphenylene)₂, a semiconducting metal–organic graphene analogue. *J. Am. Chem. Soc.* **136**, 8859–8862 (2014).
15. Dou, J.-H. et al. Signature of metallic behavior in the metal–organic frameworks M₃(hexaiminobenzene)₂ (M=Ni, Cu). *J. Am. Chem. Soc.* **139**, 13608–13611 (2017).
16. Kambe, T. et al. Redox control and high conductivity of nickel bis(dithiolene) complex π-nanosheet: a potential organic two-dimensional topological insulator. *J. Am. Chem. Soc.* **136**, 14357–14360 (2014).
17. Hmadeh, M. et al. New porous crystals of extended metal-catecholates. *Chem. Mater.* **24**, 3511–3513 (2012).
18. Ko, M., Mendecki, L. & Mirica, K. A. Conductive two-dimensional metal–organic frameworks as multifunctional materials. *Chem. Commun.* **54**, 7873–7891 (2018).
19. Smith, M. K., Jensen, K. E., Pivak, P. A. & Mirica, K. A. Direct self-assembly of conductive nanorods of metal–organic frameworks into chemiresistive devices on shrinkable polymer films. *Chem. Mater.* **28**, 5264–5268 (2016).
20. Clough, A. J. et al. Metallic conductivity in a two-dimensional cobalt dithiolene metal–organic framework. *J. Am. Chem. Soc.* **139**, 10863–10867 (2017).
21. Ziebel, M. E., Darago, L. E. & Long, J. R. Control of electronic structure and conductivity in two-dimensional metal–semiquinoid frameworks of titanium, vanadium and chromium. *J. Am. Chem. Soc.* **140**, 3040–3051 (2018).
22. Yaghi, O. M., Gandara-Barragan, F., Lu, Z. & Wan, S. Preparation of metal-catecholate frameworks. US patent 8,742,152 B2 (2014).
23. Cotton, S. A. *Lanthanide and Actinide Chemistry* (Wiley, 2006).
24. Shannon, R. Revised effective ionic radii and systematic studies of interatomic distances in halides and chalcogenides. *Acta Crystallogr. A* **32**, 751–767 (1976).
25. Xie, L. S. et al. Tunable mixed-valence doping toward record electrical conductivity in a three-dimensional metal–organic framework. *J. Am. Chem. Soc.* **140**, 7411–7414 (2018).
26. Rietveld, H. M. A profile refinement method for nuclear and magnetic structures. *J. Appl. Crystallogr.* **2**, 65–71 (1969).
27. Barrett, E. P., Joyner, L. G. & Halenda, P. P. The determination of pore volume and area distributions in porous substances. I. Computations from nitrogen isotherms. *J. Am. Chem. Soc.* **73**, 373–380 (1951).
28. Brunauer, S., Emmett, P. H. & Teller, E. Adsorption of gases in multimolecular layers. *J. Am. Chem. Soc.* **60**, 309–319 (1938).
29. Wu, B., Zinkevich, M., Aldinger, F., Wen, D. & Chen, L. Ab initio study on structure and phase transition of A- and B-type rare-earth sesquioxides Ln₂O₃ (Ln=La–Lu, Y and Sc) based on density function theory. *J. Solid State Chem.* **180**, 3280–3287 (2007).
30. Pawley, G. S. Unit-cell refinement from powder diffraction scans. *J. Appl. Crystallogr.* **14**, 357–361 (1981).
31. Trucano, P. & Chen, R. Structure of graphite by neutron diffraction. *Nature* **258**, 136–137 (1975).
32. Hoffmann, R. How chemistry and physics meet in the solid state. *Angew. Chem. Int. Ed.* **26**, 846–878 (1987).
33. Kittel, C. *Introduction to Solid State Physics* (Wiley, 2004).
34. Tauc, J. Optical properties and electronic structure of amorphous Ge and Si. *Mater. Res. Bull.* **3**, 37–46 (1968).
35. Grange, C. S., Meijer, A. J. H. M. & Ward, M. D. Trinuclear ruthenium dioxolene complexes based on the bridging ligand hexahydroxytriphenylene: electrochemistry, spectroscopy and near-infrared electrochromic behaviour associated with a reversible seven-membered redox chain. *Dalton Trans.* **39**, 200–211 (2010).
36. Welber, B., Cardona, M., Kim, C. K. & Rodriguez, S. Dependence of the direct energy gap of GaAs on hydrostatic pressure. *Phys. Rev. B* **12**, 5729–5738 (1975).
37. Müller, H., Trommer, R., Cardona, M. & Vogl, P. Pressure dependence of the direct absorption edge of InP. *Phys. Rev. B* **21**, 4879–4883 (1980).
38. Balslev, I. Influence of uniaxial stress on the indirect absorption edge in silicon and germanium. *Phys. Rev.* **143**, 636–647 (1966).
39. Nabi, Z., Abbar, B., Méçabih, S., Khalfi, A. & Amrane, N. Pressure dependence of band gaps in PbS, PbSe and PbTe. *Comput. Mater. Sci.* **18**, 127–131 (2000).
40. Sun, L., Park, S. S., Sheberla, D. & Dincă, M. Measuring and reporting electrical conductivity in metal–organic frameworks: Cd₂(TTFTB) as a case study. *J. Am. Chem. Soc.* **138**, 14772–14782 (2016).
41. DeGayner, J. A., Jeon, I.-R., Sun, L., Dincă, M. & Harris, T. D. 2D conductive iron-quinoid magnets ordering up to Tc=105 K via heterogenous redox chemistry. *J. Am. Chem. Soc.* **139**, 4175–4184 (2017).
42. Foster, M. E., Sohlberg, K., Allendorf, M. D. & Talin, A. A. Unraveling the semiconducting/metallic discrepancy in Ni₃(HITP)₂. *J. Phys. Chem. Lett.* **9**, 481–486 (2018).
43. Perdew, J. P. et al. Restoring the density-gradient expansion for exchange in solids and surfaces. *Phys. Rev. Lett.* **100**, 136406 (2008).
44. Kresse, G. & Furthmüller, J. Efficient iterative schemes for ab initio total-energy calculations using a plane-wave basis set. *Phys. Rev. B* **54**, 11169–11186 (1996).
45. Grimme, S., Antony, J., Ehrlich, S. & Krieg, H. A consistent and accurate ab initio parametrization of density functional dispersion correction (DFT-D) for the 94 elements H-Pu. *J. Chem. Phys.* **132**, 154104 (2010).

46. Grimme, S., Ehrlich, S. & Goerigk, L. Effect of the damping function in dispersion corrected density functional theory. *J. Comput. Chem.* **32**, 1456–1465 (2011).
47. Perdew, J. P. & Wang, Y. Accurate and simple analytic representation of the electron-gas correlation energy. *Phys. Rev. B* **45**, 13244–13249 (1992).

Acknowledgements

Author contributions

G.S. and M.D. planned and designed the experiments. G.S. executed the syntheses, chemical, spectroscopic and electrical characterization. G.S., B.A.T. and C.M.B. collected and analysed the PXRD data. T.W.K. and C.H.H. performed the DFT studies. All authors were involved in the writing of the manuscript and have given consent to this publication.

Competing interests

The authors declare no competing interests.

Additional information

Supplementary information is available for this paper at https://doi.org/10.1038/s41557-019-0372-0.

Correspondence and requests for materials should be addressed to M.D.

Reprints and permissions information is available at www.nature.com/reprints.

Publisher's note Springer Nature remains neutral with regard to jurisdictional claims in published maps and institutional affiliations.